CrystEngComm

ROYAL SOCIETY OF CHEMISTRY

PAPER

View Article Online
View Journal | View Issue

Cite this: *CrystEngComm*, 2025, **27**, 5337

Chiral selectivity in lithium niobate crystals: investigating the role of L- and D-alanine as chiral inducers†

Matan Oliel * and Yitzhak Mastai

Received 22nd May 2025,
Accepted 29th June 2025

DOI: 10.1039/d5ce00522a

rsc.li/crystengcomm

Lithium niobate is an achiral crystal that intriguingly exhibits chiral selectivity, as well as properties typically associated with chiral crystals such as nonlinear polarization and piezoelectricity. Here, we explore L-alanine and D-alanine as chiral inducers during the hydrothermal synthesis of $LiNbO_3$ nanocrystals. Structural and morphological analyses using X-ray diffraction, Fourier-transform infrared spectroscopy, high-resolution scanning electron microscopy, and transmission electron microscopy reveal clear differences between pristine and induced crystals. Low-frequency Raman and circular dichroism spectroscopy, high-performance liquid chromatography, and isothermal titration calorimetry were employed to investigate the chirality and enantiomeric selectivity. L-Ala-induced $LiNbO_3$ crystals preferentially adsorbed L-enantiomers, while D-Ala-induced crystals favored D-enantiomers. This study sheds light on the mechanisms of chiral induction in inorganic crystals, highlighting the potential of $LiNbO_3$ for chiral sensing, enantioselective catalysis and biomolecular recognition.

Introduction

Chirality is usually related to organic chemistry and biochemistry; however, there is a wide branch of chirality in the inorganic world. It can appear in non-centrosymmetric inorganic crystal structures with a chiral space group. There are 65 chiral space groups (Sohncke space groups) divided into two types: first-order chiral crystals that appear in nature in their chiral form (22 space groups, *e.g.* α-quartz) and second-order chiral crystals that are achiral but may become chiral by the presence of a chiral molecule during crystallization (43 space groups). All Sohncke space groups contain only operations of the first kind (rotations, roto-translations, translations).[1]

There is surprisingly little research on the chirality of chiral inorganic crystals due to complicated synthesis requiring very high temperature and pressure that are difficult to reach. However, the surface of chiral inorganic crystals shows great potential for several uses including chiral discrimination,[2–4] chiral sensing,[5] and enantioselective catalysis.[6,7] As chiral selectivity occurs mostly on the material surface, it is essential to comprehend how chiral induction affects surface chirality and to manage chirality in these materials.

Numerous studies were conducted on chiral discrimination on metal surfaces, in particular with metals that are cubic close-packed (CCP).[8,9] Remarkably, chiral properties are shown in the crystal planes of Cu (643), even though chirality is absent in the bulk metal. The mirror image of the Cu(6, 4, 3) surface – Cu(−6, −4, −3) – is obtained by kinks on the (6, 4, 3) surface plane that make it chiral, denoted by Cu(6, 4, 3)^R and Cu(6, 4, 3)^S. Their chiral selectivity is proven by desorption of *R*/*S*-propylene oxide from those surfaces. For chiral surfaces, adsorption of even a tiny chiral molecule can lead to an outstanding enantiomeric excess (ee)[4,10] due to the mechanism of its adsorption onto ligands connected to the surface or even onto the surface itself.

Many crystals investigated over time possess chiral characteristics, including minerals like quartz (SiO_2),[11] a non-chiral inorganic material that crystallizes as a conglomerate and exists in two variations, right- and left-handed. Moreover, quartz has three crystal structures that are very different from each other but are all chiral owing to their silicate skeletons that form right- or left-handed SiO_4 helices. Like quartz, there are many other chiral crystals that crystallize in non-centrosymmetric space groups.[12]

Calcite ($CaCO_3$),[13] on the other hand, is an achiral mineral that displays mirror-related faces, and is the source of many studies dealing with surface chirality of minerals. Calcite formation in the presence of D or L aspartic acid shows a

Department of Chemistry and Institute of Nanotechnology, Bar-Ilan University, 5290002 Ramat-Gan, Israel. E-mail: matanoliel5@gmail.com, Yitzhak.Mastai@biu.ac.il

† Electronic supplementary information (ESI) available: SAED, FTIR spectra, HPLC and ITC raw data of L- and D-Ala-induced $LiNbO_3$ (PDF). See DOI: https://doi.org/10.1039/d5ce00522a

different morphology of the (1, 0, 4) plane, indicating chiral recognition. The formation of gypsum ($CaSO_4{\cdot}2H_2O$) in the presence of 28 different chiral organic molecules, among them amino acids, resulted in crystals with asymmetric morphology.[14]

Wulfingite (ε-$Zn(OH)_2$)[15] (space group $P2_12_12_1$) and α-HgS (ref. 16 and 17) (space group $P3_121$) can be influenced by chiral molecules. By utilizing chiral surfactant molecules, such as penicillamine, in the synthesis of α-HgS nanoparticles, or amino acids, in the synthesis of (ε-$Zn(OH)_2$), a chiral crystal phase with a significant ee can be achieved.

Through a protracted process of chiral discrimination, some chiral minerals are thought to have had a role in the formation of homochirality in biological molecules.[18,19] Moreover, we can even see that chiral discrimination affects chemical elements like tellurium which is naturally chiral, and its chirality can be controlled by using chiral agents in the formation of tellurium nanocrystals.[20–22]

It is possible to uncover the underlying natural processes governing the essence of chiral biomolecules by exploring the complexities of chiral induction and simulating the natural crystallization conditions of chiral minerals in the presence of chiral amino acids, to achieve chiral discrimination in these systems. However, while some chiral minerals can be easily crystallized in their chiral phase using simple techniques, other chiral minerals are difficult to crystallize. Berlinite is a chiral polymorph of $AlPO_4$ that resembles quartz structurally. High temperatures are necessary for it to crystallize into the chiral phase during annealing.[23,24] Analyzing chiral induction processes is significantly hampered by these extreme circumstances.

An interesting phenomenon is the chiral induction of achiral crystals, which assume properties that exist in chiral crystals. Ag_2CO_3 and CuO are good examples: the former (space group $P12_1/m$) shows chiral selectivity when induced by arginine, while the latter (space group $C2/c$) shows helical symmetry when induced by both sodium dodecyl sulfate (SDS) as a structure-directing agent and amino alcohol as a symmetry breaking agent.[25] These examples increase the variety of possibilities that exist today for the chirality of crystals when properties that characterize chiral crystals also appear in achiral crystals thanks to chiral induction.

$LiNbO_3$ is an achiral crystal that belongs to space group $R3c$, which displays piezoelectricity and nonlinear polarization of light that characterize chiral crystals.[26–29] Therefore, we assumed that chiral selectivity can be induced and even controlled for $LiNbO_3$ crystals, similar to the induced selectivity of Ag_2CO_3 and CuO. Owing to its properties, $LiNbO_3$ is a very interesting system; its chirality and chiral selectivity could be highly significant for biology and biochemistry.

Here, we investigate the effects of chiral induction by alanine enantiomers, while crystallizing $LiNbO_3$ by a hydrothermal method, on chirality and chiral discrimination, seeking to control nanocrystal orientation and chiral selectivity. The morphology and structural changes were evaluated by X-ray diffraction (XRD), Fourier transform infrared (FTIR) spectroscopy, high-resolution scanning electron microscopy (HR-SEM), and transmission electron microscopy (TEM). The chiral properties were analyzed by direct power measurement using low-frequency Raman (LFR), chiral adsorption using circular dichroism (CD) spectroscopy, isothermal titration calorimetry (ITC) and high-performance liquid chromatography (HPLC) (Scheme 1).

Experimental methods

Materials

The following analytical grade chemicals were acquired from Sigma-Aldrich and used without further purification: L-Ala (>98%), D-Ala (>98%), DL-Ala (>99%), L-Arg (>98%), D-Arg (>98%), $LiOH{\cdot}H_2O$ (99%) and Nb_2O_5 (99.9%).

Chiral-induced $LiNbO_3$ crystal synthesis

Chiral-induced $LiNbO_3$ crystals were prepared by hydrothermal synthesis. $LiOH{\cdot}H_2O$ (10 mmol), Nb_2O_5 and L- or D-Ala (5 mmol each) were added in succession into a stainless-steel autoclave with 100 mL PTFE liner and filled 80% of the volume (80 mL) with double distilled water (DDW). The autoclave was sealed, stirred to allow better mixing of the components, and maintained at 260 °C for 24 h. The product was filtered under vacuum and washed several times with DDW and absolute ethanol to clear alanine and unreacted reactants. The white powder product was dried in an oven at 80 °C for 12 h and collected for characterization and future applications.

Characterization methods

The crystallographic structures of $LiNbO_3$ were determined by XRD using a Bruker AXS D8 Advance diffractometer with Cu Kα (λ = 1.5418 Å) operating at 40 kV/40 mA, collecting from 10 to 80°.

FTIR was performed using a Thermo Scientific Nicolet iS10 spectrometer equipped with a Smart iTR attenuated total reflectance sampler with a single bounce diamond crystal. Data were collected in the 530–4000 cm^{-1} range at a spectral resolution of 4 cm^{-1} and analyzed using OMNIC software.

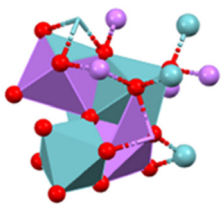

Scheme 1 $LiNbO_3$ in the $R3c$ space group: Li (violet), Nb (light blue) and O (red).

HR-SEM images were taken using a field-emission FEI (Helios 600) instrument. Samples were sputtered with gold.

Transmission electron microscopy (TEM) images were taken using a JEOL JEM-1400 microscope operated at 120 kV. Images were taken using a digital micrograph with a multiscan camera model 794 (Gatan) in different resolutions.

Methods

LFR was carried out on an inVia Raman microscope (Renishaw, UK) at room temperature (RT) under an optical microscope with a 50× objective. The samples were excited using a 514 nm laser source with a P-polarization (vertical) ratio of 100 : 1 (0.5 mW, 40 s) and spectra were acquired using a movable polarizer that can be P-polarized or S-polarized. The measurements were obtained with 1800 l mm^{-1} grating in the range of 100–500 cm^{-1}.

HPLC chiral adsorption was measured by adding a 5 mg mL^{-1} freshly prepared solution of DL-Ala in DDW to 10 mg mL^{-1} of L- or D-Ala-induced $LiNbO_3$ crystals. The crystals were kept suspended in the solution overnight using a rotary suspension mixer and filtered out using a 0.2 mm filter. The filtered solutions were subjected to HPLC measurement and compared to the control solution using an Astec Chirobiotic TAG HPLC column (5 μm particle size, 15 cm × 4.6 mm ID). The mobile phase was MeOH : H_2O 60 : 40 and the injected sample volume was 2 μL. HPLC measurements were done using a BETA 10 Plus Gradient Pump (Ecom, Czech Republic), a SAPPHIRE 800 UV-vis Variable Wavelength DETECTOR at a wavelength of 210 nm, and a DEGASSEX MODEL DG-4400 degasser (Phenomenex, Torrance, CA, USA).

CD chiral adsorption was measured by preparing 2.5 mM solutions of L- and D-Arg in DDW and adding them to 10 mg mL^{-1} of L or D-Ala-induced $LiNbO_3$ crystals. The crystals were kept suspended in solution overnight using a rotary suspension mixer and were filtered out using a 0.2 mm filter. The filtered solutions were subjected to CD measurement and compared to the control L- and D-Arg solutions at RT using a 5 mL quartz cuvette and Chirascan spectrometer (Applied Photophysics, UK).

ITC chiral adsorption was measured using 5 mM solutions of L- and D-Arg in DDW for the syringe (80 μL) and 10 mg mL^{-1} of L- or D-Ala-induced $LiNbO_3$ crystal suspension in DDW after 10 min of sonication for the sample cell (1.4 mL). The reference cells were filled with DDW (1.4 mL). Each consecutive 5 μL injection lasted 8.5 s, with an interval of 400 s between injections. The cell was stirred constantly at a rate of 300 rpm, and the reference power was 5 μcal s^{-1}. Prior to measurement, the solutions were degassed under vacuum using a ThermoVac (MicroCal) for 5 min at 25 °C to remove air bubbles. The results were analyzed using Origin software.

Results and discussion

To learn about our $LiNbO_3$ nanocrystals and the effect of the chiral induction, we used XRD. In all samples, the main morphology of $LiNbO_3$ was the RT stable trigonal phase with

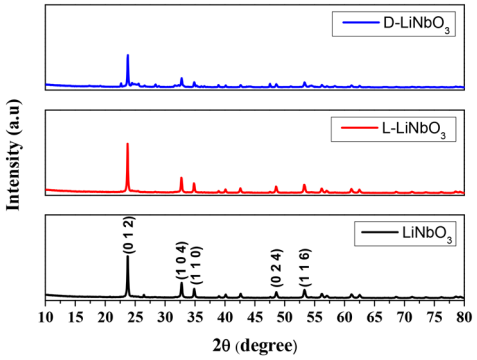

Fig. 1 XRD of the control and chiral-induced crystals at 2θ = 10–80° showing the diffraction planes of trigonal $LiNbO_3$.

the space group *R*3*c* (COD ID: 8103744) and main diffraction at 2θ = 23.8° corresponding to its (0, 1, 2) plane (Fig. 1). The cell units *a*, *b*, and *c* were 5.1381, 5.1381, and 13.8481 Å, with $\alpha = \beta = 90°$ and $\gamma = 120°$. The diffraction obtained by L-Ala-induced $LiNbO_3$ (red) is fitted to the diffraction that appears in the database, which means that it is the purest compared to the pristine and D-Ala-induced $LiNbO_3$ crystals. The small reflection at 26.5° for $LiNbO_3$ (black) and two tiny reflections at 24.5° and 27.6° for D-Ala-induced $LiNbO_3$ (blue) corresponding to the diffraction of Nb_2O_5 indicate an incomplete reaction in these cases. Clearly, the crystal structure is preserved after L- or D-Ala chiral induction. The (1, 1, 0) plane is clearly evident in the selected area electron diffraction (SAED) images of both induced crystals (see Fig. S1†).

The Scherrer equation $D = \frac{K\lambda}{\beta \cos\theta}$ was applied to the five most intense XRD reflections to calculate the average particle size: *K* is a dimensionless shape factor (0.89), λ is the X-ray wavelength (0.15406 nm), β is the net line broadening (subtracting the instrumental broadening) at half the maximum intensity, and θ is the Bragg angle (both in radians). The calculations show an increase in size as a result of the chiral induction, by 10–12% (75 *vs.* 84 nm for L-Ala and 82 nm for D-Ala, see Table 1). Similar reflection ratios indicate no change of preference to different planes during crystallization as a result of the chiral induction. Moreover, the weaker intensities of the D-Ala-induced $LiNbO_3$ crystals compared to those of the control $LiNbO_3$ and L-Ala-induced $LiNbO_3$ crystals result from the lower sample quality.

FTIR spectroscopy was used to characterize the as-synthesized $LiNbO_3$ (Fig. S2†). The spectra for pure and D/L-Ala-induced $LiNbO_3$ were the same, showing the desired Nb–O vibration band at 562 cm^{-1}. No other peaks are observed in the spectra, indicating that the product is clean from any traces of alanine.

The morphology and surface of the crystals were examined by HR-SEM as presented in Fig. 2. Both non-induced and L-chiral-induced $LiNbO_3$ crystals show a structure of mesocrystals[30,31] made up of nm-sized building blocks, arranged in a regular, repeating pattern. Mesocrystals are

Table 1 Dominant reflections and sizes (by XRD) of $LiNbO_3$ crystals

$LiNbO_3$	Plane	Intensity	2θ	FWHM	Size (nm)	Average size (nm)
	(0, 1, 2)	23 801.45	23.77	0.22613	77	75
	(1, 0, 4)	8191.5	32.77	0.25414	74	
	(1, 1, 0)	4815.328	34.89	0.24523	79	
	(0, 2, 4)	3042.3	48.59	0.33732	71	
	(1, 1, 6)	4203.106	53.31	0.31865	83	
L-$LiNbO_3$	Plane	Intensity	2θ	FWHM	Size (nm)	Average size (nm)
	(0, 1, 2)	27 081.2	23.74	0.20416	85	84
	(1, 0, 4)	8376.02	32.74	0.23661	80	
	(1, 1, 0)	5143.255	34.86	0.22577	86	
	(0, 2, 4)	3376.629	48.56	0.29764	81	
	(1, 1, 6)	4332.208	53.28	0.30725	86	
D-$LiNbO_3$	Plane	Intensity	2θ	FWHM	Size (nm)	Average size (nm)
	(0, 1, 2)	18 102.58	23.78	0.20102	86	82
	(1, 0, 4)	4526.962	32.78	0.26023	73	
	(1, 1, 0)	2624.061	34.89	0.23178	84	
	(0, 2, 4)	1559.819	48.6	0.26676	90	
	(1, 1, 6)	2467.739	53.32	0.33537	79	

constructed of small, organized nanocrystals that can be joined in many ways, as opposed to typical crystals, made up of a continuous lattice of atoms or molecules. The pristine $LiNbO_3$ mesocrystals are arranged by small nanometric crystals on top of larger ones (both rhombic) in a way that resembles terraces with an average size of ~300 nm, and sharp vertex crystal blocks (I). The addition of the amino acid as a chiral inducer conserved the arrangement of the mesocrystalline structure, but minor differences in morphology are indicated. Addition of L-Ala to $LiNbO_3$ crystals cause small deformation in the rhombic crystals which is reflected in less pointed vertices compared to the un-induced $LiNbO_3$ crystals, although no change in crystal size was detected (average of ~300 nm) (II). D-Chiral-induced $LiNbO_3$ rhombic crystals show similar deformation of crystal morphology like the L-chiral-induced $LiNbO_3$ crystals. Moreover, differences in arrangement were indicated which are reflected in a matrix arrangement, and without size change (average of ~300 nm) (III).

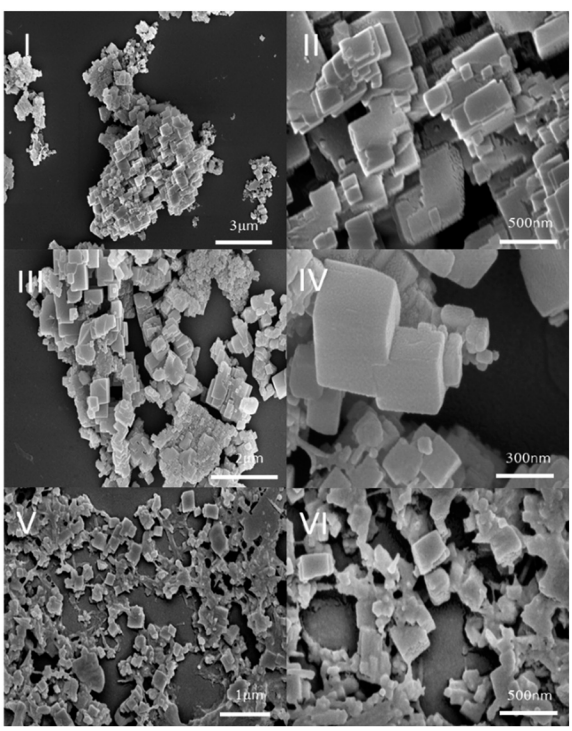

Fig. 2 HR-SEM images of the control (I/II), L-Ala-induced (III/IV) and D-Ala-induced (V/VI) $LiNbO_3$ crystals.

After learning about the induced crystalline and morphological changes, we examined the chirality and chiral selectivity. Some techniques to examine the chirality and selectivity of inorganic systems involve direct measurements, while others are indirect. Direct measurements include methods like LFR, solid and powder CD spectroscopy, and even second-harmonic generation (SHG),[32–34] which provide solid proof for the chirality of the crystals; however, there is great difficulty finding the conditions for such measurement. Indirect methods like adsorption and crystallization experiments allow checking the selectivity of the chiral inorganic systems by techniques such as polarimetry, CD, ITC and HPLC; however, these methods do not provide information about the crystals themselves.

To study our chiral-induced $LiNbO_3$, we used the LFR method to measure its chirality directly. The LFR method is a typical Raman measurement that allows the measurement of the chirality of crystals at low frequencies in the addition of an optical polarizer.[35–38] In this measurement, polarized light hits the sample, and the collected excited light passes through the optical polarizer to the detector to give Raman signals. In chirality measurements, chiral molecules and chiral crystals give different signal intensities when they are perpendicularly/parallelly polarized (S-Pol/P-Pol). To prove the

chirality, the enantiomer should give stronger intensity for S-Pol, while its co-enantiomer should show the opposite phenomenon – stronger signals for P-Pol. The crystals are excited, and the collected light passes through an optical polarization at S-Pol and P-Pol.

The LFR spectrum of the $LiNbO_3$ crystal shows typical peaks at 151 cm^{-1} corresponding to the ETO_1 mode, at 237 cm^{-1} corresponding to the ETO_2 mode (the strongest vibration mode), and at 365 cm^{-1} corresponding to the ETO_3 mode.[39–41] In general, ETO modes are transverse optical vibrations in the *xy* plane of the crystal. The ETO_1 and ETO_2 modes describe deformations/titling of oxygen octahedra combined by cationic displacements in the *xy* plane and ETO_3 mode describe tilting of the oxygen octahedra.[42] In our measurements, we focused on the 237 cm^{-1} frequency because it is the most intense peak of the $LiNbO_3$ LFR scattering, and the P/S-polarization effect is the strongest at this mode. For un-induced $LiNbO_3$ crystals, no difference in intensities are indicated when the light has been collected at S-Pol/P-Pol throughout the spectrum with 99.6% overlap. When the light was collected at S-Pol, L-Ala-induced $LiNbO_3$ crystals showed a higher intensity than when the light was collected at P-Pol throughout the spectrum with a maximum intensity ratio of 1.25 at the strongest vibration mode (237 cm^{-1}, Fig. 3II). As expected, the co-enantiomer D-Ala-induced $LiNbO_3$ crystals showed the opposite phenomenon – higher intensity with light collected at P-Pol throughout the spectrum with a maximum intensity ratio of 1.28 (237 cm^{-1}, Fig. 3III).

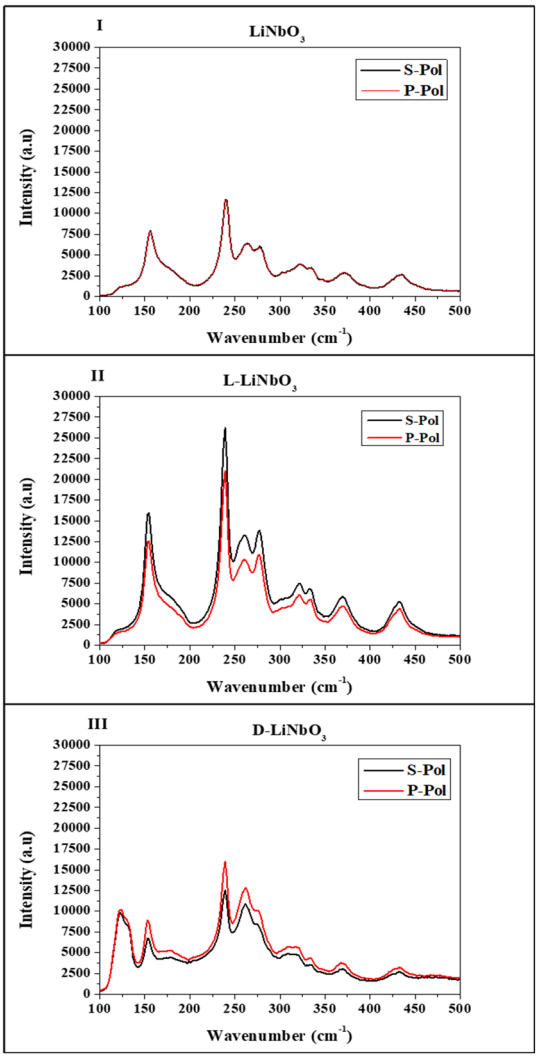

Fig. 3 LFR spectra of un-induced (I), L-Ala-induced (II) and D-Ala-induced (III) $LiNbO_3$. Black/red curves present signals excited using S/P-Pol.

LFR represents long-range interactions, where polarizable interactions are orientation-dependent. These long-range interactions are particularly sensitive to changes in the symmetry of the excitation cone induced by the polarizer. Therefore, in a measurement performed in this spectral region, observation of the phenomenon, in which the intensity of light collected from a chiral material varies as a function of the collection angle (S-Pol/P-Pol), allows us to distinguish and prove the chirality of $LiNbO_3$.

CD allows the checking of the chirality of solutions and powders by using circular polarization.[43–45] In CD measurements, the chirality of the molecule is determined by measuring the absorbance difference between left- and right-handed circular light, providing the molar CD. The measurements help to prove chiral selectivity using adsorption experiments by determining the CD ratio between the enantiomer adsorbed on the crystal surface and the pure enantiomer. As the concentration is related to peak intensity, the disparity was taken to represent the quantity of chiral molecules adsorbed onto the crystal surface.

Fig. 4I presents the CD of D/L-Arg adsorbed onto un-induced $LiNbO_3$ and onto chiral-induced $LiNbO_3$ at a concentration of 10 mg mL^{-1}. As expected, the L- and D-Arg CD after adsorption onto un-induced $LiNbO_3$ doesn't present any chiral selectivity between the enantiomers compared to the pure L- and D-Arg (Fig. 4II). In contrast, L-Ala-induced $LiNbO_3$ crystals show better adsorption for L-Arg (62%, red curve) compared to pure L-Arg (black), while D-Arg shows absorbance of 44% onto L-Ala-induced $LiNbO_3$ (cyan) compared to pure D-Arg (pink). The arginine enantiomers show selectivity to the L-induced crystals, with better selectivity to L-Arg at all concentrations with a maximal selectivity of 18% (Fig. 4III). On the other hand, the D-Ala-induced $LiNbO_3$ crystals show a better adsorption of 54% (green) for D-Arg and 41% for L-Arg compared to the pure enantiomers. The selectivity of the Arg enantiomers towards D-Ala-$LiNbO_3$ reveals a notable preference for D-Arg at all concentrations, with a maximum selectivity of 13% (Fig. 4IV). Moreover, the difference in selectivity between the enantiomers changes only slightly in both L- and D-Ala-induced $LiNbO_3$ crystals at increasing crystal concentrations.

For the chiral HPLC measurements, we checked the induced $LiNbO_3$ chiral selectivity adsorption in the DL-Ala racemic mixture by using a chiral column. HPLC allows separating and quantifying different materials in a mixture.

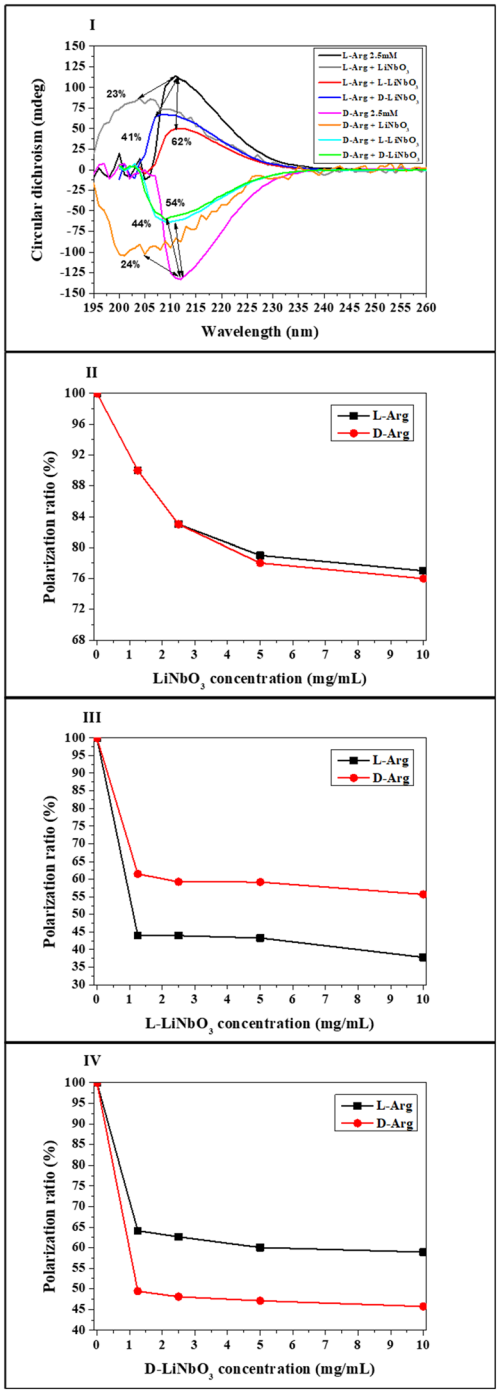

Fig. 4 Selective chiral adsorption of Arg on chiral-induced $LiNbO_3$ crystals – CD spectra of L- and D-Arg adsorbed onto L- or D-Ala-induced $LiNbO_3$ crystals (I). Selectivity curves of L- and D-Arg at different crystal concentrations induced by un-induced $LiNbO_3$ (II), L-Ala-induced $LiNbO_3$ (III) or D-Ala-induced $LiNbO_3$ (IV).

In chiral selectivity measurements, a chiral column can separate the D and L enantiomers in racemic mixtures (the enantiomers exit the column at different times), allowing us to track the changes in the ratio between the quantities of each enantiomer, which is related to their peak area. In adsorption experiments, if one enantiomer is adsorbed more

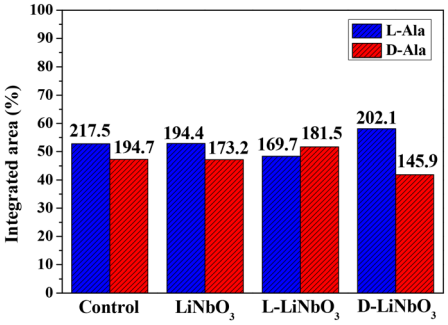

Fig. 5 Selective chiral adsorption of alanine on un-induced and chiral-induced $LiNbO_3$ crystals measured by HPLC equipped with a chiral column.

to the crystal than its co-enantiomer, its relative quantity in the remaining solution would be lower, changing the ratio between the enantiomers.

Fig. 5 presents the adsorption of the DL-Ala racemic mixture onto un-induced and L- or D-Ala-induced $LiNbO_3$. The control measurement was a racemic solution of DL-Ala with no crystals. The solution contained 52.77% L-Ala (217.5 mAU s) and 47.23% D-Ala (194.7 mAU s). The sample that was suspended with un-induced $LiNbO_3$ showed a peak area decrease of 10.62% for L-Ala (194.4 mAU s) and 11.04% for D-Ala (173.2 mAU s). The solution contained 52.88% L-Ala (47.12% D-Ala) which means that although there is adsorption of alanine to the $LiNbO_3$ crystals, the adsorption isn't selective at all.

In the sample suspended with L-Ala-induced $LiNbO_3$, the solution contained 48.32% L-Ala (51.68% D-Ala). The peak area change in the L-Ala-induced $LiNbO_3$ sample was −22.12% for L-Ala and −7.18% for D-Ala, a chiral selectivity of ~14.9% in favor of L-Ala.

The sample suspended with the D-Ala-induced $LiNbO_3$ solution contained 58.08% L-Ala (41.92% D-Ala). The peak area change is thus −6.91% for L-Ala and −25.64% for D-Ala – a chiral selectivity of ~18.7% in favor of D-Ala (Fig. 5). The HPLC chromatograms of DL-Ala before and after adsorption onto un-induced and L- or D-Ala-induced $LiNbO_3$ are shown in Fig. S3.†

The chiral selectivity adsorption of the L- or D-Ala-induced $LiNbO_3$ crystals was examined by ITC, selecting arginine for the adsorption. ITC allows us to measure enthalpy changes at good resolution by titration. The instrument includes a syringe containing the titrant, a sample cell for the titrand, and a reference cell for the solvent. While titrating, a reaction occurs, heat is usually released or consumed, and the temperature in the sample cell changes. The thermostat applies an electric voltage equal to the heat change to keep both cells at the same temperature, and the feedback appears as a peak signal in the ITC curve.

In chirality measurements, small enantiomer molecules titrate into a suspension of chiral crystals, and the enthalpy change (ΔH) differences between both enantiomers indicate selective adsorption onto the crystal surface.[44–53] Fig. 6

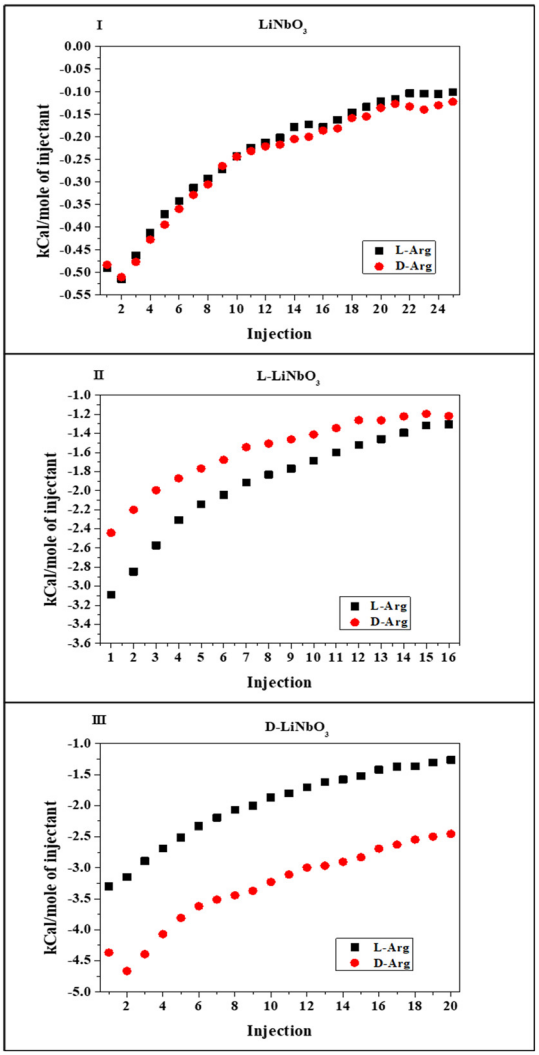

Fig. 6 Calculated selective chiral adsorption of Arg on induced $LiNbO_3$ – enthalpy changes of L- and D-Arg onto crystals: un-induced (I) and induced by L-Ala (II) and D-Ala (III).

presents the total enthalpy per injection after integration, normalizing from the raw measurement graph (Fig. S4†). The results in Fig. 6I present the enthalpy for the titration of L- and D-Arg into un-induced $LiNbO_3$, showing very low enthalpy change values and no chiral selectivity at all. When we titrated L- and D-Arg into L-Ala-induced $LiNbO_3$ the L-Arg shows significantly stronger adsorption (average = −1.926 kcal mol^{-1}) compared to D-Arg (−1.587 kcal mol^{-1}). The energy difference between the enantiomers is 0.339 kcal mol^{-1}, a selectivity of 17.6% in favor of L-Arg (Fig. 6II). As expected, Fig. 6III presents the opposite trend: D-Arg adsorbs much more strongly onto D-Ala-induced $LiNbO_3$ crystals (−3.498 kcal mol^{-1}) compared to L-Arg (−2.166 kcal mol^{-1}), a highly significant energy difference (the difference between both enantiomers is 1.332 kcal mol^{-1}), corresponding to a selectivity of 38.1% in favor of D-Arg. The adsorption is thus much better, with more than two-fold greater selectivity compared to the L-Ala-induced $LiNbO_3$ crystals.

Conclusions

Overall, this study demonstrates that alanine successfully induces chirality in $LiNbO_3$ nanocrystals, leading to distinct morphological and surface modifications. The main change that occurred was reflected in the arrangement of the crystals. The L-Ala-induced $LiNbO_3$ crystals exhibited a terrace arrangement, whereas the D-Ala-induced $LiNbO_3$ crystals resemble a matrix arrangement. For both of them, no significant size change has been indicated and rhombic morphology crystals have been obtained, as expected due the space group. The chirality of the induced crystals was confirmed through low-frequency Raman (LFR) spectroscopy, which revealed distinct optical responses indicative of enantioselective interactions. Further chiral selectivity experiments using circular dichroism (CD) spectroscopy, high-performance liquid chromatography (HPLC), and isothermal titration calorimetry (ITC) demonstrated that L-Ala-induced $LiNbO_3$ preferentially adsorbs L-enantiomers, while D-Ala-induced $LiNbO_3$ favors D-enantiomers. ITC results further revealed stronger enantioselective interactions in D-Ala-induced $LiNbO_3$ compared to its L-Ala counterpart. These findings highlight the ability of amino acids to induce chirality in inorganic crystals, expanding the potential applications of such materials as tunable platforms for chiral discrimination, enantioselective catalysis, and chiral sensing. Moreover, the capacity to control chirality in an originally achiral inorganic crystal through molecular induction provides valuable insights into chiral selection mechanisms, which are relevant to both prebiotic chemistry and the development of novel functional materials. This study deepens our understanding of the interactions between chiral molecules and inorganic surfaces, opening new avenues for the design of chiral-responsive materials with broad applications in chemistry and nanotechnology.

Data availability

The data supporting the findings of this study are available within the article and its ESI† materials. Additional raw data can be provided by the corresponding author upon reasonable request.

Conflicts of interest

There are no conflicts to declare.

Acknowledgements

MO acknowledges the Institute for Nanotechnology and Advanced Materials at Bar-Ilan University for his Bar-Ilan President's Ph.D. Scholarship.

Notes and references

1 R. M. Hazen, *Chiral Crystal Faces of Common Rock-Forming Minerals*, Woodhead Publishing Limited, 2004.

2 C. Wattanakit, Y. B. Saint Côme, V. Lapeyre, P. A. Bopp, M. Heim, S. Yadnum, S. Nokbin, C. Warakulwit, J. Limtrakul and A. Kuhn, Enantioselective Recognition at Mesoporous Chiral Metal Surfaces, *Nat. Commun.*, 2014, **5**, 1–8.

3 W. Xu, M. Cheng, S. Zhang, Q. Wu, Z. Liu, M. K. Dhinakaran, F. Liang, E. G. Kovaleva and H. Li, Recent Advances in Chiral Discrimination on Host-Guest Functionalized Interfaces, *Chem. Commun.*, 2021, **57**(61), 7480–7492.

4 D. S. Sholl, A. Asthagiri and T. D. Power, Naturally Chiral Metal Surfaces as Enantiospecific Adsorbents, *J. Phys. Chem. B*, 2002, **105**(21), 4771–4782.

5 J. D. Horvath and A. J. Gellman, Enantiospecific Desorption of Chiral Compounds from Chiral Cu(643) and Achiral Cu(111) Surfaces, *J. Am. Chem. Soc.*, 2002, **124**(10), 2384–2392.

6 C. E. Song and S. G. Lee, Supported Chiral Catalysts on Inorganic Materials, *Chem. Rev.*, 2002, **102**(10), 3495–3524.

7 A. Matsumoto, Y. Kaimori, M. Uchida, H. Omori, T. Kawasaki and K. Soai, Achiral Inorganic Gypsum Acts as an Origin of Chirality through Its Enantiotopic Surface in Conjunction with Asymmetric Autocatalysis, *Angew. Chem., Int. Ed.*, 2017, **56**(2), 545–548.

8 A. J. Gellman, Chiral Surfaces: Accomplishments and Challenges, *ACS Nano*, 2010, **4**(1), 5–10.

9 C. F. McFadden, P. S. Cremer and A. J. Gellman, Adsorption of Chiral Alcohols on "Chiral" Metal Surfaces, *Langmuir*, 1996, **12**(10), 2483–2487.

10 Ž. Šljivančanin, K. V. Gothelf and B. Hammer, Density Functional Theory Study of Enantiospecific Adsorption at Chiral Surfaces, *J. Am. Chem. Soc.*, 2002, **124**(49), 14789–14794.

11 Y. Tanaka, T. Takeuchi, S. W. Lovesey, K. S. Knight, A. Chainani, Y. Takata, M. Oura, Y. Senba, H. Ohashi and S. Shin, Right Handed or Left Handed? Forbidden X-Ray Diffraction Reveals Chirality, *Phys. Rev. Lett.*, 2008, **100**(14), 1–4.

12 D. Avnir, Chirality in Minerals, *Minerals*, 2024, **14**(10), 995.

13 W. Jiang, M. S. Pacella, Di Athanasiadou, V. Nelea, H. Vali, R. M. Hazen, J. J. Gray and M. D. McKee, Chiral Acidic Amino Acids Induce Chiral Hierarchical Structure in Calcium Carbonate, *Nat. Commun.*, 2017, **8**, 1–13.

14 G. Otis, M. Nassir, M. Zutta, A. Saady, S. Ruthstein and Y. Mastai, Enantioselective Crystallization of Chiral Inorganic Crystals of ε-Zn(OH)2 with Amino Acids, *Angew. Chem., Int. Ed.*, 2020, **59**(47), 20924–20929.

15 J. Gao, H. Li, Z. Sun, J. Song, Y. Liu, C. Jin, Z. Zhang, J. A. Ma and W. Jiang, Selective Chiral Recognition between Amino Acids and Growing Gypsum Crystals, *Lngmuir*, 2023, **39**(36), 12707–12714.

16 A. Ben-Moshe, A. O. Govorov and G. Markovich, Enantioselective Synthesis of Intrinsically Chiral Mercury Sulfide Nanocrystals, *Angew. Chem.*, 2013, **125**(4), 1313–1317.

17 R. M. Hazen, Mineral Surfaces and the Prebiotic Selection and Organization of Biomolecules, *Am. Mineral.*, 2006, **91**(11–12), 1715–1729.

18 R. M. Hazen and D. A. Sverjensky, Mineral Surfaces, Geochemical Complexities, and the Origins of Life, *Cold Spring Harbor Perspect. Biol.*, 2010, **2**(5), a002162.

19 R. M. Hazen, T. R. Filley and G. A. Goodfriend, Selective Adsorption of L- and D-Amino Acids on Calcite: Implications for Biochemical Homochirality, *Proc. Natl. Acad. Sci. U. S. A.*, 2001, **98**(10), 5487–5490.

20 A. Ben-Moshe, A. da Silva, A. Muller, A. Abu-Odeh, P. Harrison, J. Waelder, F. Niroui, C. Ophus, A. M. Minor, M. Asta, W. Theis, P. Ercius and A. P. Alivisatos, The Chain of Chirality Transfer in Tellurium Nanocrystals, *Science*, 2021, **372**(6543), 729–733.

21 F. Calavalle, M. Suárez-Rodríguez, B. Martín-García, A. Johansson, D. C. Vaz, H. Yang, I. V. Maznichenko, S. Ostanin, A. Mateo-Alonso, A. Chuvilin, I. Mertig, M. Gobbi, F. Casanova and L. E. Hueso, Gate-Tuneable and Chirality-Dependent Charge-to-Spin Conversion in Tellurium Nanowires, *Nat. Mater.*, 2022, **21**(5), 526–532.

22 T. Furukawa, Y. Watanabe, N. Ogasawara, K. Kobayashi and T. Itou, Current-Induced Magnetization Caused by Crystal Chirality in Nonmagnetic Elemental Tellurium, *Phys. Rev. Res.*, 2021, **3**(2), 1–14.

23 Y. Muraoka and K. Kihara, The Temperature Dependence of the Crystal Structure of Berlinite, a Quartz-Type Form of AlP04, *Phys. Chem. Miner.*, 1997, **24**(4), 243–253.

24 J. C. Jumas, A. Goiffon, B. Capelle, A. Zarka, J. C. Doukhan, J. Schwartzel, J. Détaint and E. Philippot, Crystal Growth of Berlinite, AlPO4: Physical Characterization and Comparison with Quartz, *J. Cryst. Growth*, 1987, **80**(1), 133–148.

25 Y. Duan, X. Liu, L. Han, S. Asahina, D. Xu, Y. Cao, Y. Yao and S. Che, Optically Active Chiral CuO "Nanoflowers", *J. Am. Chem. Soc.*, 2014, **136**(20), 7193–7196.

26 R. A. Ganeev, I. A. Kulagin, A. I. Ryasnyansky, R. I. Tugushev and T. Usmanov, Characterization of Nonlinear Optical Parameters of KDP, LiNbO3 and BBO Crystals, *Opt. Commun.*, 2004, **229**(1–6), 403–412.

27 N. M. Bityurin, V. I. Bredikhin and V. N. Genkin, Nonlinear Optical Absorption and Energy Structure of LiNbO 3 and α-LiIO 3 Crystals, *Sov. J. Quantum Electron.*, 1978, **8**(11), 1377–1379.

28 W. Yue and J. Yi-Jian, Crystal Orientation Dependence of Piezoelectric Properties in LiNbO3 and LiTaO3, *Opt. Mater.*, 2003, **23**(1–2), 403–408.

29 F. Chen, L. Kong, W. Song, C. Jiang, S. Tian, F. Yu, L. Qin, C. Wang and X. Zhao, The Electromechanical Features of LiNbO3 Crystal for Potential High Temperature Piezoelectric Applications, *J. Materiomics*, 2019, **5**(1), 73–80.

30 M. Niederberger and H. Cölfen, Oriented Attachment and Mesocrystals: Non-Classical Crystallization Mechanisms Based on Nanoparticle Assembly, *Phys. Chem. Chem. Phys.*, 2006, **8**(28), 3271–3287.

31 X. Xia, J. Tu, Y. Zhang, X. Wang, C. Gu, X. B. Zhao and H. J. Fan, High-Quality Metal Oxide Core/Shell Nanowire Arrays on Conductive Substrates for Electrochemical Energy Storage, *ACS Nano*, 2012, **6**(6), 5531–5538.

32 J. J. Maki, M. Kauranen and A. Persoons, Surface Second-Harmonic Generation from Chiral Materials, *Phys. Rev. B: Condens. Matter Mater. Phys.*, 1995, **51**(3), 1425–1434.
33 M. Kauranen, T. Verbiest, J. J. Maki and A. Persoons, Second-Harmonic Generation from Chiral Surfaces, *J. Chem. Phys.*, 1994, **101**(9), 8193–8199.
34 S. Huang, Q. Qian, R. Zu, Q. Ji, G. S. Jung, K. Zhang, Y. Zhang, M. J. Buehler, J. Kong and V. Gopalan, Chirality-Dependent Second Harmonic Generation of MoS2nanoscroll with Enhanced Efficiency, *ACS Nano*, 2020, **14**(10), 13333–13342.
35 V. H. Damle, H. Aviv and Y. R. Tischler, Identification of Enantiomers Using Low-Frequency Raman Spectroscopy, *Anal. Chem.*, 2022, **94**(7), 3188–3193.
36 H. Aviv, I. Nemtsov, Y. Mastai and Y. R. Tischler, Characterization of Crystal Chirality in Amino Acids Using Low-Frequency Raman Spectroscopy, *J. Phys. Chem. A*, 2017, **121**(41), 7882–7888.
37 I. Nemtsov, Y. Mastai, Y. R. Tischler and H. Aviv, Chiral Purity of Crystals Using Low-Frequency Raman Spectroscopy, *ChemPhysChem*, 2018, **19**(22), 3116–3121.
38 I. Nemtsov, H. Aviv, Y. Mastai and Y. R. Tischler, Polarization Dependence of Low-Frequency Vibrations from Multiple Faces in an Organic Single Crystal, *Crystals*, 2019, **9**(8), 425.
39 K. Chen, Y. Li, C. Peng, Z. Lu, X. Luo and D. Xue, Microstructure and defect characteristics of lithium niobate with different Li concentrations, *Inorg. Chem. Front.*, 2021, **8**(17), 4006–4013.
40 Y. Bao, T. Chen, Z. Miao, W. Zheng, P. Jiang, K. Chen, R. Guo and D. Xue, Machine-Learning-Assisted Understanding of Depth-Dependent Thermal Conductivity in Lithium Niobate Induced by Point Defects, *Adv. Electron. Mater.*, 2025, 2400944.
41 S. Sanna, A. Riefer, S. Neufeld, W. G. Schmidt, G. Berth, M. Rüsing, A. Widhalm and A. Zrenner, Vibrational fingerprints of LiNbO3-LiTaO3 mixed crystals, *Ferroelectrics*, 2013, **447**(1), 63–68.
42 M. Rüsing, S. Sanna, S. Neufeld, G. Berth, W. G. Schmidt and A. Zrenner, Vibrational properties of LiNb1−xTaxO3 mixed crystals, *Phys. Rev. B*, 2016, **93**, 184305.
43 X. T. Kong, L. V. Besteiro, Z. Wang and A. O. Govorov, Plasmonic Chirality and Circular Dichroism in Bioassembled and Nonbiological Systems: Theoretical Background and Recent Progress, *Adv. Mater.*, 2020, **32**(41), 1–14.
44 S. Allenmark, Induced Circular Dichroism by Chiral Molecular Interaction, *Chirality*, 2003, **15**(5), 409–422.
45 G. Gottarelli, S. Lena, S. Masiero, S. Pieraccini and G. P. Spada, The Use of Circular Dichroism Spectroscopy for Studying the Chiral Molecular Self-Assembly: An Overview, *Chirality*, 2008, **20**(3), 471–485.
46 A. Shval and Y. Mastai, Isothermal Titration Calorimetry as a New Tool to Investigate Chiral Interactions at Crystal Surfaces, *Chem. Commun.*, 2011, **47**(20), 5735–5737.
47 M. Shinitzky, A. Shvalb, A. C. Elitzur and Y. Mastai, Entrapped Energy in Chiral Solutions: Quantification and Information Capacity, *J. Phys. Chem. B*, 2007, **111**(37), 11004–11008.
48 C. Dryzun, Y. Mastai, A. Shvalb and D. Avnir, Chiral Silicate Zeolites, *J. Mater. Chem.*, 2009, **19**(14), 2062.
49 L. Werber and Y. Mastai, Isothermal Titration Calorimetry for Chiral Chemistry, *Chirality*, 2018, **30**(5), 619–631.
50 L. C. Preiss, L. Werber, V. Fischer, S. Hanif, K. Landfester, Y. Mastai and R. Muñoz-Espí, Amino-Acid-Based Chiral Nanoparticles for Enantioselective Crystallization, *Adv. Mater.*, 2015, **27**(17), 2728–2732.
51 L. Lugasi, I. Grinberg, S. Rudnick-Glick, E. Okun, H. Einat and S. Margel, Designed Proteinoid Polymers and Nanoparticles Encapsulating Risperidone for Enhanced Antipsychotic Activity, *J. Nanobiotechnol.*, 2020, **18**(1), 1–16.
52 J. Kardos, K. Yamamoto, K. Hasegawa, H. Naiki and Y. Goto, Direct Measurement of the Thermodynamic Parameters of Amyloid Formation by Isothermal Titration Calorimetry, *J. Biol. Chem.*, 2004, **279**(53), 55308–55314.
53 M. Oliel and Y. Mastai, Heat of Dilution and Racemization of Chiral Amino Acid Solutions, *J. Solution Chem.*, 2024, **53**(12), 1701–1714.